Efficient Photoelectrochemical Hydrogen Generation Based on Core Size Effect of Heterostructured Quantum Dots

Kanghong Wang, Yi Tao, Zikun Tang, Xiaolan Xu, Daniele Benetti, François Vidal, Haiguang Zhao,* Federico Rosei,* and Xuhui Sun**

Colloidal quantum dots (QDs) are shown to be effective as light-harvesting sensitizers of metal oxide semiconductor (MOS) photoelectrodes for photoelectrochemical (PEC) hydrogen (H_2) generation. The CdSe/CdS core/shell architecture is widely studied due to their tunable absorption range and band alignment via engineering the size of each composition, leading to efficient carrier separation/transfer with proper core/shell band types. However, until now the effect of core size on the PEC performance along with tailoring the core/shell band alignment is not well understood. Here, by regulating four types of CdSe/CdS core/shell QDs with different core sizes (diameter of 2.8, 3.1, 3.5, and 4.8 nm) while the thickness of CdS shell remains the same (thickness of 2.0 ± 0.1 nm), the Type II, Quasi-Type II, and Type I core/shell architecture are successfully formed. Among these, the optimized CdSe/CdS/TiO2 photoelectrode with core size of 3.5 nm can achieve the saturated photocurrent density (J_{ph}) of 17.4 mA cm^{-2} under standard one sun irradiation. When such cores are further optimized by capping alloyed shells, the J_{ph} can reach values of 22 mA cm^2 which is among the best-performed electrodes based on colloidal QDs.

1. Introduction

Converting solar energy into electricity or chemical fuels is a promising approach to address the issues of ever-growing global energy demand and environmental pollution. In particular, solar-driven PEC cells can be used to generate H_2 from water by splitting it into oxygen (O_2) and H_2 in a low-cost and environmentally friendly way.[1–6] Generally, a PEC cell for H_2 production consists of a photoanode, a (photo)cathode (counter-electrode), and an electrolyte. Typically, the most widely used photoanodes are made of *n*-type MOS (i.e., TiO_2, ZnO, Fe_2O_3, SnO_2, etc.),[7–10] thanks to their stability against photo/chemical corrosion. However, MOS-based PEC devices suffer from low solar-to-hydrogen (STH) efficiency due to their limited light absorption range and/or high recombination rates.

To broaden the absorption range, QDs have been widely used to sensitize the MOS thus forming a heterostructure, widening the absorption range for solar-driven PEC H_2 generation.[11–15] The colloidal QDs are preferred as light harvesters due to their superior optoelectronic properties: i) size-/composition- tunable bandgap; ii) wide absorption range and high absorption coefficient; iii) the possibility of multiple exciton generation with single photon absorption, etc.[16,17] However, bare QDs present an unstable surface which may become a major source of nonradiative recombination center for carriers, limiting the optoelectronic performance and stability.

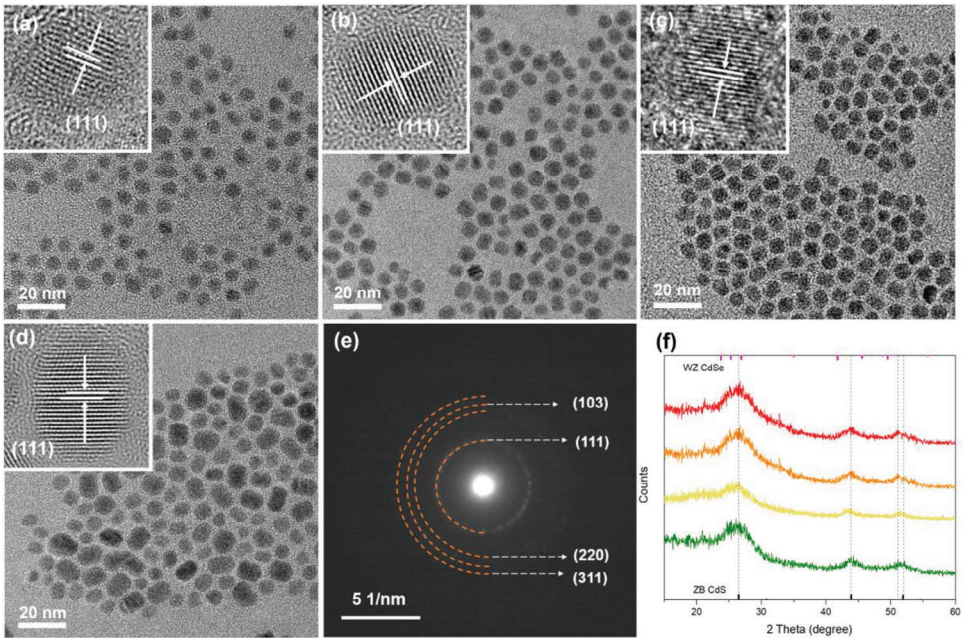

Figure 1. TEM images and HR-TEM images (insets) of the corresponding QDs: a) CdSe (2.8 nm)/CdS QDs, b) CdSe (3.1 nm)/CdS QDs, c) CdSe (3.5 nm)/CdS QDs, d) CdSe (4.8 nm)/CdS QDs; e) Representative SAED pattern of CdSe (3.5 nm)/CdS QDs, f) XRD pattern of CdSe (2.8 nm)/CdS QDs, CdSe (3.1 nm)/CdS QDs, CdSe (3.5 nm)/CdS QDs, CdSe (4.8 nm)/CdS QDs.

To solve this issue, core/shell architectures have been reported in which a shell of another semiconductor material is grown on the surface of the QD seed.[12,18,19] Such architecture passivates the QDs' surface by epitaxial growth of another semiconductor and also allows for tuning of the band alignment between the core and shell, leading to a more efficient carrier separation/transfer.[20–24] Up-to-date, numerous core/shell QDs structures have been used in optoelectronic devices, such as PbS/CdS,[25–27] CdSe/CdS,[28–30] CdS/CdSe,[31–33] CuInSe/CuInS,[34–36] etc. For example, Jin et al.[25] reported a PbS/CdS core/shell QDs-based photoanode for the application of PEC H_2 generation, achieving a saturated photocurrent density (J_{ph}) of 11.2 mA cm^{-2} under one sun illumination (AM 1.5 G, 100 mW cm^{-2}). Recently, Zhang et al.[31] reported a CdS/CdSe core/shell architecture by tuning the shell thickness of CdSe, achieving a J_{ph} of 16 mA cm^{-2} in a solar-driven PEC cell.

While eco-friendly QDs have been proposed as alternatives,[37–39] until now the CdSe/CdS core/shell structure is still the most efficient architecture for PEC devices, thanks to its favorable band alignment for efficient carrier transfer as well as absorption range which overlaps with the visible range of the solar spectrum. Moreover, the small lattice mismatch (≈3.9%) between CdSe and CdS also plays an important role in reducing defects at the interfaces and thus yielding a higher conversion efficiency.[40,41]

While the majority of studies focused on engineering the CdS shell, by either tuning its thickness or its composition,[28,42,43] the size effect of the CdSe core and accordingly the core/shell band alignment for the improvement of PEC cell have not been explored yet. According to the size-tunable properties of QDs, the bandgap will become narrower with a larger core size (size below its Bohr Radius),[11,44] indicating that the charge transfer efficiency can be affected significantly due to the band offset between the core and shell. At the same time, the absorption range will also be largely impacted by the different QD core sizes. Moreover, CdSe/CdS core/shell architecture is promising toward optimizing the performance of optoelectronic devices by tuning the core/shell types into Type I, Type II, and Quasi-Type II through core size engineering.

Herein, we report four CdSe/CdS core/shell QDs, denoted as CdSe (2.8, 3.1, 3.5, 4.8 nm)/CdS, in which we retained similar values of the shell thickness (thickness of 2.0 ± 0.1 nm) while the core sizes were varied as 2.8, 3.1, 3.5, and 4.8 nm, respectively. These four types of CdSe/CdS core/shell QDs were then used as sensitizers of mesoporous TiO_2 photoanodes. After additional ligand exchange and capping with two monolayers of ZnS, the photoanodes were evaluated for current density-voltage (J–V) curves and stability performance under standard one sun illumination (AM 1.5 G, 100 mW cm^{-2}). The J_{ph} was found to be strongly dependent on the CdSe core size, exhibiting 8.2 mA cm^{-2} for CdSe (2.8 nm)/CdS QDs, 15.8 mA cm^{-2} for CdSe (3.1 nm)/CdS QDs, 17.4 mA cm^{-2} for CdSe (3.5 nm)/CdS QDs and 12.9 mA cm^{-2} for CdSe (4.8 nm)/CdS QDs, respectively. These findings indicate that by optimizing the absorption range and band alignment of CdSe/CdS core/shell QDs via precise size control, the PEC performance can be improved dramatically, yielding an increase of J_{ph} by 53%. Furthermore, based on the optimized core size (diameter of 3.5 nm), alloyed intermediate shells were added to further accelerate the carrier transfer efficiency, leading to an unprecedented J_{ph} value of 22 mA cm^{-2} under one sun illumination. Overall, these results indicate a promising route for highly efficient and low-cost photoanode for H_2 production.

Table 1. QDs size and absorption/PL peak position.

QDs	Diameter [nm]	Abs peak [nm]	PL peak [nm]
CdSe (2.8 nm)	2.8 ± 0.2	537	552
CdSe (3.1 nm)	3.1 ± 0.2	550	566
CdSe (3.5 nm)	3.5 ± 0.3	571	580
CdSe (4.8 nm)	4.8 ± 0.3	605	621
CdSe (2.8 nm)/CdS	6.6 ± 0.6	585	595
CdSe (3.1 nm)/CdS	7.1 ± 0.7	605	615
CdSe (3.5 nm)/CdS	7.7 ± 0.7	608	618
CdSe (4.8 nm)/CdS	8.9 ± 1.2	635	648

2. Results and Discussion

The CdSe core QDs were synthesized via a hot-injection approach following a typical protocol with some modification.[45] The core size is fixed by controlling the reaction time (details in the experimental section) after precursor injection. According to the empirical mathematical functions (calculated from exciton peak in UV–Vis spectra which are shown in supporting information), the core size obtained for 1, 2.5, 3.5, and 5 min reactions are 2.8, 3.1, 3.5, and 4.8 nm, respectively.[23] Afterward, the CdS shell was grown on the surface of the core by the SILAR method. In this particular case, for all the core QDs the shell thickness was maintained equally by applying the same six SILAR cycles and adjusting accordingly the precursor amount (see Table S1, Supporting Information).[46] Typically, the obtained four representative types of CdSe/CdS core/shell QDs with different core sizes were denoted as CdSe (2.8 nm)/CdS QDs, CdSe (3.1 nm)/CdS QDs, CdSe (3.5 nm)/CdS QDs and CdSe (4.8 nm)/CdS QDs, respectively. The histogram of size dispersion for four core QDs and four core/shell QDs is shown in Figures S2 and S3 (Supporting Information). The optical images of all four types of QDs are shown in Figure S4 (Supporting Information) under sunlight and UV light for comparison.

In **Figure** 1a–d, the transmission electron microscopy (TEM) images show the CdSe (2.8 nm)/CdS QDs, CdSe (3.1 nm)/CdS QDs and CdSe (3.5 nm)/CdS QDs all have monodispersed size. However, the size of CdSe (4.8 nm)/CdS QDs varies largely which is mainly due to the large surface area of CdSe core QDs of CdSe (4.8 nm)/CdS QDs. The average sizes of four core/shell QDs are listed in **Table 1**. The insets in the images (a–d) display that all the QDs have high crystallization in the high-resolution TEM (HR-TEM) images and all the lattice spacings correspond to (111) planes of zinc blende (ZB) crystal structure of CdS. This result is consistent with previous reports[29,47] which is attributed to the thick CdS shell in "Giant" CdSe/CdS QDs. Figure 1e shows the selected area electron diffraction (SAED) pattern of CdSe (3.5 nm)/CdS QDs which indicates that the lattice distance corresponds to the (111), (220), (103), and (311) planes of ZB CdS, in good agreement with HR-TEM results. In addition, Figure S5 (Supporting Information) shows SAED patterns of the other three types of CdSe/CdS core/shell QDs, revealing the same results.

To further verify the structure of QDs, XRD patterns of four samples were acquired (Figure 1f). According to the XRD patterns, all four CdSe/CdS core/shell QDs have wurtzite (WZ) crystal structure for the CdSe core and ZB crystal structure for the CdS shell, in agreement with TEM images. The minor difference is that QD with a larger core size tends to show WZ CdSe crystal structure while QD with a smaller core exhibits ZB CdS crystal structure due to the relatively thick shell. In summary, the different reaction time of the seed growth does not change the crystal structure of the QDs.

As shown in the HR-TEM (In Figure S6, Supporting Information), white circles indicate the position of the QDs, revealing that the EPD process[48] was successful in depositing CdSe (3.5 nm)/CdS QDs onto mesoporous TiO_2 films. Further investigations using cross-sectional SEM and energy dispersive spectroscopy (EDS) confirmed the uniform dispersion of the four CdSe/CdS QDs within the mesoporous TiO_2 sheets (shown in Figures S7–S10, Supporting Information).

The optical properties of as-prepared QDs were further investigated by UV-Vis absorption spectroscopy and PL spectroscopy. According to the UV–Vis absorption spectra, the first-exciton absorption peak is located at 537, 550, 571, and 605 nm, respectively for four CdSe core QDs (**Figure** 2a). The absorption range was broadened by increasing the core size, as expected. After six SILAR cycles of CdS layers, all the first-exciton absorption peaks are red-shifted to longer wavelengths up to 585, 605, 608, and 635 nm, respectively, which indicates the successful epitaxy growth of CdS on the surface of CdSe (Figure 2b).[49] Similar phenomena are observed for PL spectra as shown in Figure 2c and the values of the position of the peaks are all shown in Table 1 for comparison.

To investigate the carrier dynamic behavior of four types of core/shell QDs, transient PL decay measurements were acquired using QDs dispersed on different substrates. As shown in Figure 2d, the PL spectra indicate the average lifetimes of QDs with TiO_2 (black curve), ZrO_2 (blue curve), and ZrO_2 in electrolyte (green curve). The average lifetime τ can be determined through the following equation:[50]

$$\langle\tau\rangle = \frac{a_1\tau_1^2 + a_2\tau_2^2 + a_3\tau_3^2}{a_1\tau_1 + a_2\tau_2 + a_3\tau_3} \quad (1)$$

where a_i (i = 1, 2, 3) is the fitting coefficient and τ_i (i = 1, 2, 3) is the characteristic lifetime. The ZrO_2 was used as the benchmark for comparison with the TiO_2 substrate where the electron injection from QDs to ZrO_2 does not occur due to unfavorable band alignment. Thus, the PL decay can be assigned to charge recombination inside the QDs.[37] The electron and hole transfer rate can be calculated according to the following equation:

$$K_{et/ht} = \frac{1}{\langle\tau\rangle QDs - TiO_2/ZrO_2\ (electrolyte)} - \frac{1}{\langle\tau\rangle QDs - ZrO_2} \quad (2)$$

where K_{et} and K_{ht} refer to the transfer rate of electrons and holes, respectively. $<\tau>$ QDs-TiO_2, $<\tau>$ QDs-ZrO_2 and $<\tau>$ QDs-ZrO_2 (electrolyte) reflects the average lifetime of QDs on the substrates of TiO_2, ZrO_2, QDs-ZrO_2 with electrolyte, respectively. In such a system, the energy transfer between QDs was neglected.[29,50] All the lifetime values are listed in **Table 2**. The CdSe (2.8 nm)/CdS QDs, with the smallest core size, exhibit the fastest electron transfer rate of 3.8×10^7 s^{-1}, consistent with the previous results that the band alignment of core and shell for this type of

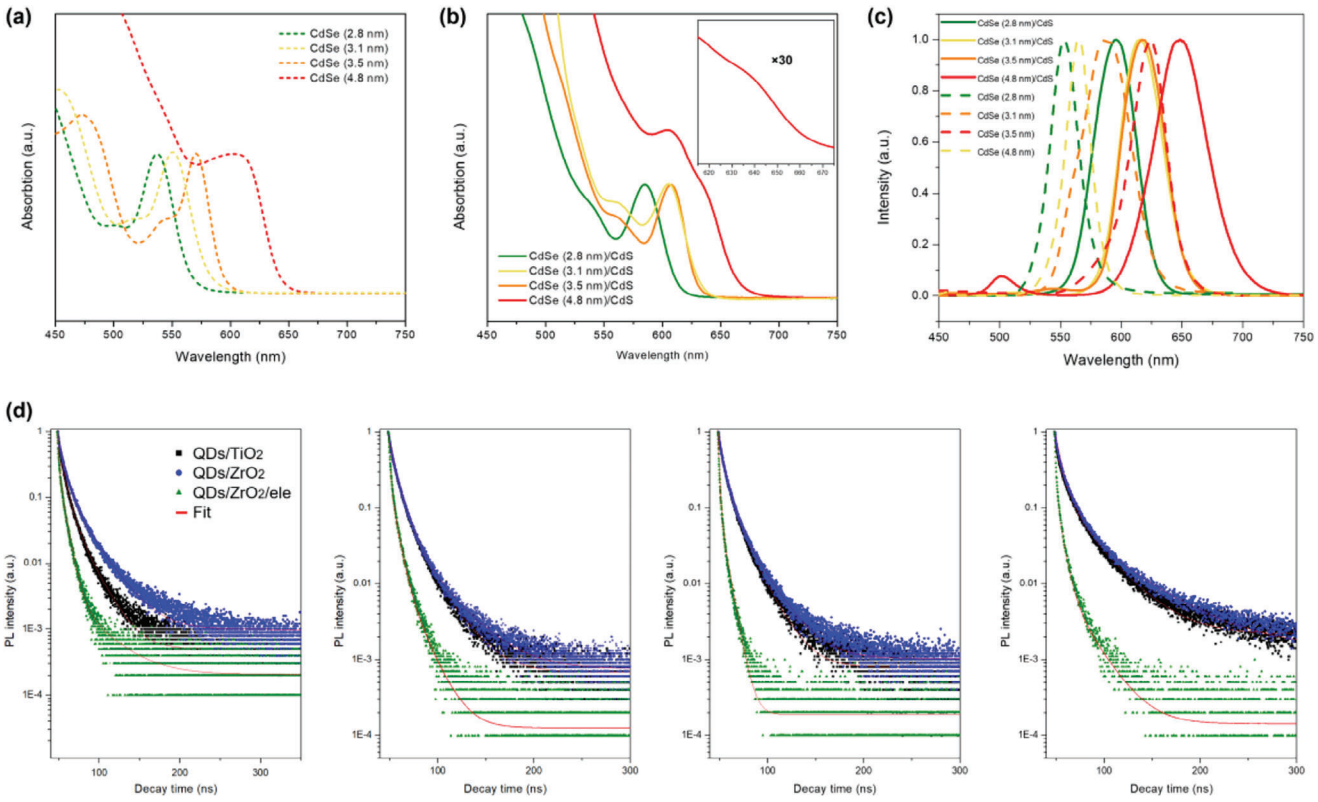

Figure 2. UV-Vis absorption spectra of QDs in toluene: a) CdSe (2.8 nm) QDs, CdSe (3.1 nm) QDs, CdSe (3.5 nm) QDs, CdSe (4.8 nm) QDs; b) CdSe (2.8 nm)/CdS QDs, CdSe (3.1 nm)/CdS QDs, CdSe (3.5 nm)/CdS QDs, CdSe (4.8 nm)/CdS QDs; c) PL spectra of CdSe (2.8 nm), CdSe (3.1 nm), CdSe (3.5 nm), CdSe (4.8 nm) core QDs (dash line) and corresponding CdSe/CdS core/shell QDs (solid line) in toluene; d) Transient PL spectra of CdSe (2.8 nm)/CdS QDs, CdSe (3.1 nm)/CdS QDs, CdSe (3.5 nm)/CdS QDs, CdSe (4.8 nm)/CdS QDs on TiO_2 films (black square), ZrO_2 films (Blue circle) and ZrO_2 films with electrolyte (green triangle).

QD are most favorable for charge transfer. CdSe (3.1 nm)/CdS QDs and CdSe (3.5 nm)/CdS QDs show similar electron transfer rates of 0.5×10^7 s^{-1} and 0.8×10^7 s^{-1}, respectively. For CdSe (4.8 nm)/CdS QDs, the largest core size, the electron transfer rate is estimated as -0.4×10^7 s^{-1} which is a negative value. Such a phenomenon means less opportunity for electrons from core to shell which can be attributed to a narrow bandgap of the CdSe core with a large bandgap of CdS shell, leading to unfavorable band alignment for the electrons to transfer to the shell regions. In summary, when increasing the CdSe core size, the bandgap of the CdSe core becomes smaller, leading to a lower electron transfer efficiency from the core to the shell.

The Fermi level (FL) and maximal valence band (VB) energy level (E_{VB}) of the four CdSe core QDs were measured using ultraviolet photoelectron spectroscopy (UPS) with He I radiation (21.21 eV). The minimum conduction band (CB) energy level (E_{CB}) was calculated by combining the UPS results and the absorption spectra.[51,52] The energy levels of the CdSe core are determined by the UPS results while the energy levels of CdS use −3.3 and −5.8 eV as E_{CB} and E_{VB} which is the CdS bulk materials' levels, following previous studies.[25,29] The band alignment between the core and shell was analyzed through the relative band edge of CB which dramatically impacts the K_{et}. Due to the strong driving force from the electrolyte (pH ≈13), the influence of K_{ht} from band alignment was neglected. Figure S11 (Supporting Information) and **Table 3** show the UPS analysis of four types of CdSe core. From the UPS data, the Fermi level (E_F) of four core QDs is located at −2.81 eV for CdSe (2.8 nm) QDs, −3.41 eV for CdSe (3.1 nm) QDs, −4.11 eV for CdSe (3.5 nm) QDs and −4.51 eV for CdSe (4.8 nm) QDs, respectively, respect

Table 2. Average PL lifetime of as-synthesized QDs/MOS and the corresponding charge transfer rate.

QDs	QDs with TiO_2 [ns]	QDs with ZrO_2 [ns]	QDs with electrolyte [ns]	K_{et} [10^7 s^{-1}]	K_{ht} [10^7 s^{-1}]
CdSe (2.8 nm)/CdS	8.6	12.8	6.7	3.8	7.1
CdSe (3.1 nm)/CdS	10.9	11.5	4.8	0.5	12.4
CdSe (3.5 nm)/CdS	9.9	10.8	4.3	0.8	14.1
CdSe (4.8 nm)/CdS	15.2	14.4	3.9	−0.4	18.9

Table 3. Potential (respect to vacuum) of CB, VB and Fermi level for different QDs following the UPS.

QDs	E_h [eV]	E_l [eV]	E_F [eV]	E_{VB} [eV]	E_{CB} [eV]	Band gap [eV]
CdSe (2.8 nm)	18.40	2.30	−2.81	−5.11	−2.80	2.31
CdSe (3.1 nm)	17.80	2.24	−3.41	−5.66	−3.40	2.26
CdSe (3.5 nm)	17.10	2.10	−4.11	−6.21	−4.04	2.17
CdSe (4.8 nm)	16.70	1.80	−4.51	−6.31	−4.26	2.05

of vacuum level according to the high energy cut-off (E_h). While the low energy cut-off (E_l) of 2.1 eV indicates the maximum VB at −5.11, −5.66, −6.21, and −6.31 eV for four QDs. According to these data and the estimation of the bandgap from the Tauc plot, the minimum CB is located at −2.8, −3.4, −4.04, and −4.26 eV for four QDs, respectively. All the energy levels are summarized in **Figure** 3a and Table 3. The tauc plot (Figure S12, Supporting Information) was further calculated from UV–Vis spectra to estimate the bandgap of CdSe cores, confirming the results of UPS (<0.09 eV). Figure 3a also exhibits the CdSe/CdS core/shell structure and the corresponding band position of four core/shell QDs. According to the figure, the bandgap of CdSe QDs becomes narrower with a larger size. Thus, the core/shell band alignment is changed from Type II to Quasi-Type II, consistent with the PL lifetime results.

To further verify the carrier dissociation behavior of four types of CdSe/CdS core/shell QDs, the theoretical electron-hole wave functions were calculated based on solving the calculated stationary Schrödinger equation in a 3D spherical geometry.[37,47]

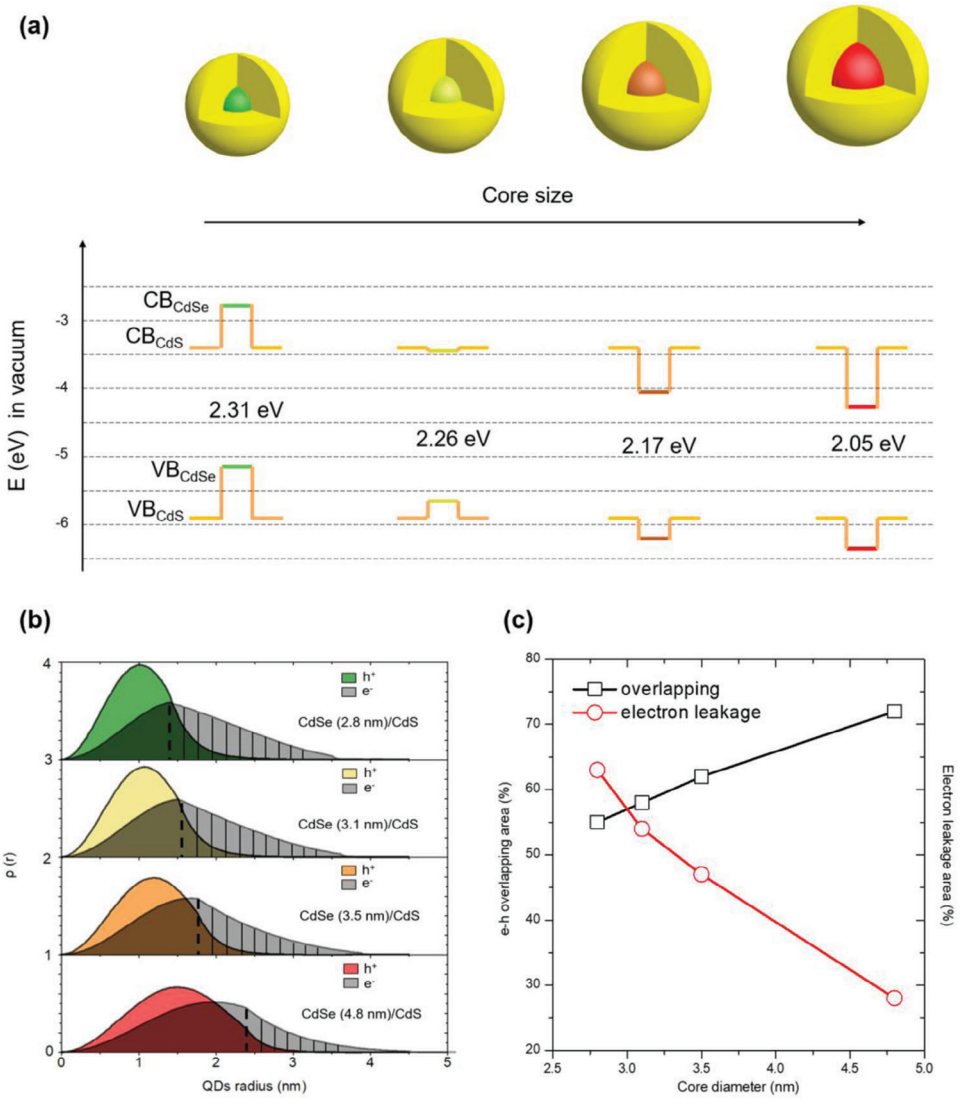

Figure 3. a) Schematic of CdSe (2.8 nm)/CdS QDs, CdSe (3.1 nm)/CdS QDs, CdSe (3.5 nm)/CdS QDs, CdSe (4.8 nm)/CdS QDs with the increasing core size and their band position (conduction/valence band) calculated following the UPS results; b) Spatial probability distribution value $\rho(r)$ of electrons and holes as a function of QD radius (nm) for CdSe (2.8 nm)/CdS QDs, CdSe (3.1 nm)/CdS QDs, CdSe (3.5 nm)/CdS QDs, CdSe (4.8 nm)/CdS QDs (dashed lines show the radius position and the shadow areas indicate the electrons in the shell regions); c) The overlapping area and electron leakage area as the function of core radius.

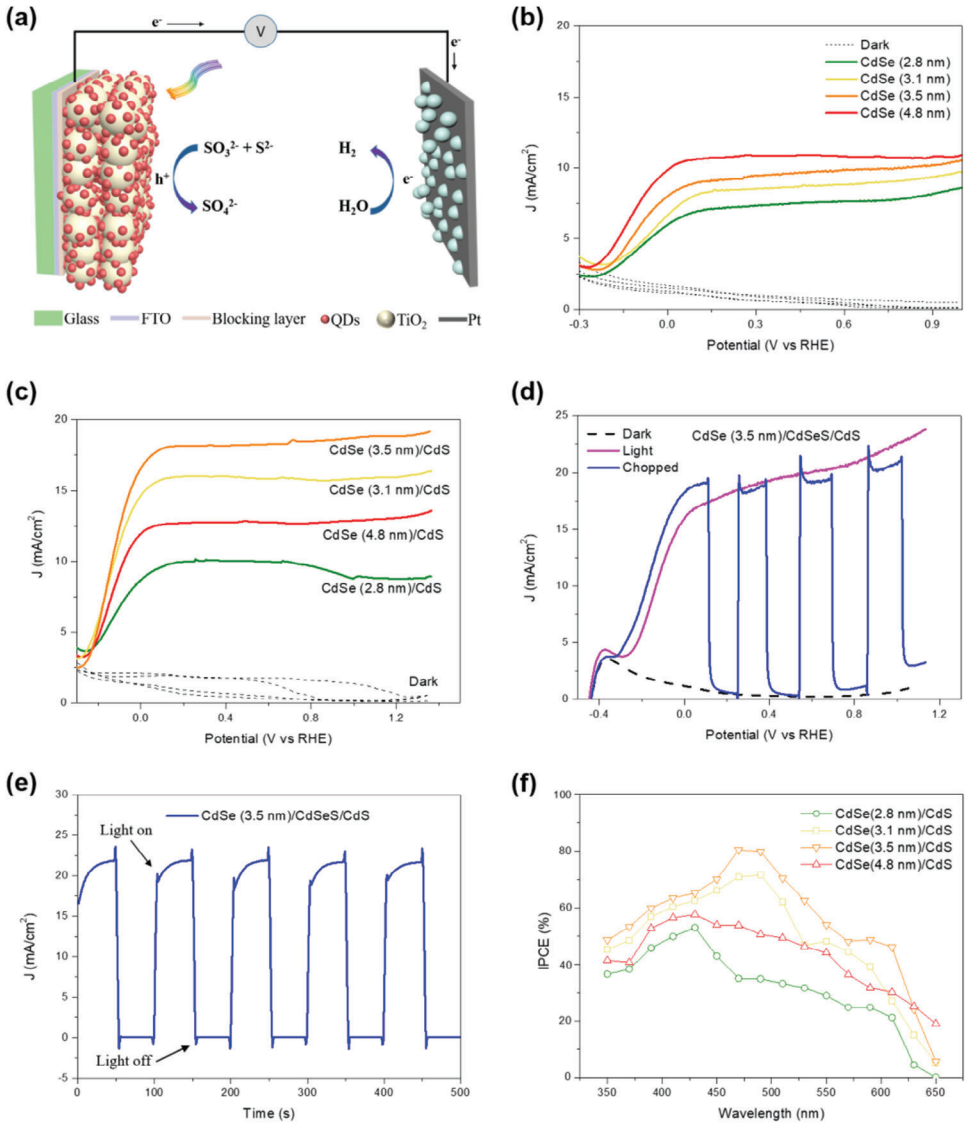

Figure 4. a) Schematic diagram of PEC device based on mesoporous TiO_2 films sensitized with QDs; Photocurrent density-potential dependence curve: b) TiO_2 sensitized with CdSe (2.8 nm) QDs, CdSe (3.1 nm) QDs, CdSe (3.5 nm) QDs, CdSe (4.8 nm) QDs; c) TiO_2 sensitized with CdSe (2.8 nm)/CdS QDs, CdSe (3.1 nm)/CdS QDs, CdSe (3.5 nm)/CdS QDs, CdSe (4.8 nm)/CdS QDs in the dark (black dash curve) and under continuous (chromatic solid curve) illumination (AM 1.5 G, 100 mW cm^{-2}); d) TiO_2 sensitized with alloyed CdSe/CdSeS/CdS QDs in the dark (black curve), under continuous (magenta curve) and chopped (blue curve) illumination; e) Photo photocurrent density versus time of alloyed CdSe/CdSeS/CdS QDs; f) IPCE spectra of photoanodes on mesoporous TiO_2 films sensitized with CdSe (2.8 nm)/CdS QDs, CdSe (3.1 nm)/CdS QDs, CdSe (3.5 nm)/CdS QDs, CdSe (4.8 nm)/CdS QDs.

Typically, the electron [$\psi_e(r)$] and hole [$\psi_h(r)$] wave functions in a 3D dot for the four types of core/shell QDs represent the possibility of carrier occupation. Figure 3b shows the $\psi_e(r)$ and $\psi_h(r)$ as a function of core radius and the vertical dashed lines indicate the position of the core radius for each QDs and the shadow areas (areas on the right of the dashed lines) show the probability of the electron leaking from the core to the shell regions. Figure 3c shows the electron/hole overlapping areas of four types of QDs and the electron leakage area as a function of core size. The overlapping area increases with the larger core size, consistent with previous results which show that the electrons have a higher probability of being confined in the core with increasing core size.[53,54] Such results are similar to the previous illustration that fewer electrons can leak into the shell regions when the core size increases. All the values are shown in Table S2 (Supporting Information) for comparison.

Figure 4a depicts the working mechanism of a PEC cell for H_2 evolution based on QDs/TiO_2 photoanode. Generally, a PEC cell consists of a QD-based photoanode, a Pt counter-electrode, and a strong-alkaline electrolyte (Na_2S/Na_2SO_3, pH ≈13). Upon solar irradiation, the QDs absorb photons and generate electron/hole pairs. These excitons will be dissociated at the QDs/TiO_2 interfaces: the electron will be injected into the CB of TiO_2 due to the favorable band alignment, while the holes on the surface of the

Table 4. PEC and stability performance of four CdSe core QDs and four CdSe/CdS core/shell QDs.

QDs	J_{ph} [mA cm^{-2}]	Retention after 2 [%]
CdSe (2.8 nm)	7.4	/
CdSe (3.1 nm)	8.5	/
CdSe (3.5 nm)	9.6	/
CdSe (4.8 nm)	10.5	/
CdSe (2.8 nm)/CdS	8.2	61
CdSe (3.1 nm)/CdS	15.8	58
CdSe (3.5 nm)/CdS	17.4	56
CdSe (4.8 nm)/CdS	12.9	50
CdSe (3.5 nm)/CdSeS/CdS	22.0	41

QDs will be consumed by the Na_2S/Na_2SO_3 electrolyte (pH ≈13). The electrons will then transfer into the FTO substrate and further travel to the counter-electrode to produce H_2 on the surface of Pt electrode.

To assess the PEC performance, four CdSe core QDs and four CdSe/CdS core/shell QDs have been deposited into mesoporous TiO_2 films for solar-driven H_2 generation. Typically, two cycles of the ligand exchange process and two SILAR cycles of the ZnS protective layer were also applied before the measurement after the 2-h EPD procedure for each QD (as detailed in the experimental section). The PEC devices under dark and continuous light illumination (AM 1.5 G 100 mW cm^{-2}) were finally measured using a typical three-electrode setup, where QDs-based photoanodes serve as working electrodes), Ag/AgCl (saturated with KCl solution) electrode as reference electrode and Pt plate serves as counter electrode. The PEC performance based on core QDs and core/shell QDs are shown in Figure 4b,c. The J_{ph} at 0.8 V versus RHE for four CdSe core QDs is 7.4 mA cm^{-2} for CdSe (2.8 nm) QDs, 8.5 mA cm^{-2} for CdSe (3.1 nm) QDs, 9.6 mA cm^{-2} for CdSe (3.5 nm) QDs and 10.5 mA cm^{-2} for CdSe (4.8 nm) QDs, respectively. Such performance indicates that the J_{ph} increases with the increase of CdSe core size which is mainly due to enhanced absorption range afforded the larger QDs. In other words, for bare CdSe QDs, the dominant parameter for PEC performance is the absorption range since there is no shell effect.

For four types of CdSe/CdS core/shell QDs, the J_{ph} of CdSe (2.8 nm)/CdS QDs-based photoanode can reach 8.2 mA cm^{-2} under one sun illumination (AM 1.5 G, 100 mW cm^{-2}). Whereas the J_{ph} of CdSe (3.1 nm)/CdS QDs-based photoanode increased up to 15.8 mA cm^{-2}, two times higher compared to the CdSe (2.8 nm)/CdS QDs-based photoanode. Moreover, for CdSe (3.5 nm)/CdS QDs-based photoanode, J_{ph} can reach a remarkable value of 17.4 mA cm^{-2}, comparable even to PEC devices that use alloyed gradient core/shell QDs.[55–58] However, the CdSe (4.8 nm)/CdS QDs-based photoanode shows only a slight improvement compared to bare QDs, with J_{ph} values of 12.9 mA cm^{-2}. This value is also lower than that of CdSe (3.1 nm)/CdS and CdSe (3.5 nm)/CdS QDs. All the J_{ph} values for QDs are listed in **Table 4** and **Figure 5c** for comparison.

For relatively small CdSe cores, below 4 nm, the absorption is still the dominant parameter for PEC performance. In fact, even though the electron transfer rate is much higher for CdSe (2.8 nm)/CdS QDs compared to CdSe (3.1 nm)/CdS and CdSe (3.5 nm)/CdS QDs, the PEC performance is still lower due to the narrower absorption range. However, when the CdSe core is large enough, above 4 nm, the absorption is no longer the dominant factor for PEC performance. In fact, the J_{ph} of CdSe (4.8 nm)/CdS QDs based photoanode is much lower than CdSe (3.1 nm)/CdS and CdSe (3.5 nm)/CdS QDs based photoanodes. This is mainly due to the fact that the carrier transfer efficiency becomes the most relevant parameter to dominate the PEC performance. Even though the absorption of CdSe (4.8 nm)/CdS QDs is stronger than CdSe (3.1 nm)/CdS and CdSe (3.5 nm)/CdS QDs, the electron transfer rate is much lower, leading to more electron-hole recombination inside of QDs, and to an overall reduction in the J_{ph}. Thus, the CdSe (3.5 nm)/CdS QDs presented the optimum compromise between absorption and charge transfer, thanks to an optimized core size as well as appropriate band alignment of the CdSe/CdS architecture. To further improve the PEC performance based on the optimized core size, alloyed layers were then applied to replace the pure CdS shells, forming a structure of CdSe (3.5 nm)/$(CdSe_xS_{1-x})_5$/CdS QDs (x = 0.5) QDs (denoted as CdSe/CdSeS/CdS QDs). These newly formed alloyed QDs were then used as sensitizers for mesoporous TiO_2 films for PEC analysis. According to Figure 4c,d, the J_{ph} of alloyed QDs-based photoanode can achieve an impressive value of 22 mA cm^{-2} under one sun illumination (AM 1.5 G, 100 mW cm^{-2}) which is one of the highest values reported for QDs-based photoanodes. Several studies with high J_{ph} are listed in Table S3 (Supporting Information). Figure 4d displays a chronoamperometric test of the alloyed QDs/TiO_2 photoanode, conducted to evaluate the photo-response performance in light on/off conditions. This result is consistent with the *J*–V curve that J_{ph} is ≈22 mA cm^{-2} under light conditions and the photo-response is rapid after the switch of the light on/off.

The superior J_{ph} obtained can be attributed to the presence of the alloyed shell that allows further optimization of the band alignment between the core and shell of the QDs. From the transient PL spectra of alloyed QDs (Figure S13, Supporting Information), the as-calculated K_{et} increased up to 2.9×10^7 s^{-1}, 3.6 times higher compared to CdSe (3.5 nm)/CdS QDs which demonstrates that the intermediate alloyed layers can in fact serve as short carrier pathways, leading to a more efficient carrier separation and transfer. As a result, the recombination inside QDs can be largely suppressed.[24] Under various monochromatic wavelengths, the incident photon-to-electron conversion efficiencies (IPCE) spectra of four as-prepared core-shell QDs with varied core sizes have been obtained. In Figure 4f, the optimized CdSe (3.5 nm)/CdS QDs-device exhibits almost overall higher IPCE values from 350 to 610 nm compared to the other three QDs-based photoanodes, suggesting more efficient photon-to-electron conversion, which is consistent with PEC performance. The IPCE value of CdSe (4.8 nm)/CdS QDs-based photoanode is higher than the other three QDs in longer wavelength which is mainly due to the broader absorption range originating from the larger core size.

Another crucial factor for PEC devices is the stability performance. The stability test was performed with a bias of 0.8 V versus RHE under continuous illumination. Due to the long exposure under continuous illumination and strong alkaline electrolyte (pH ≈13), a protection layer is required on the QD surface. Thus, two monolayers of ZnS passivation layers were grown

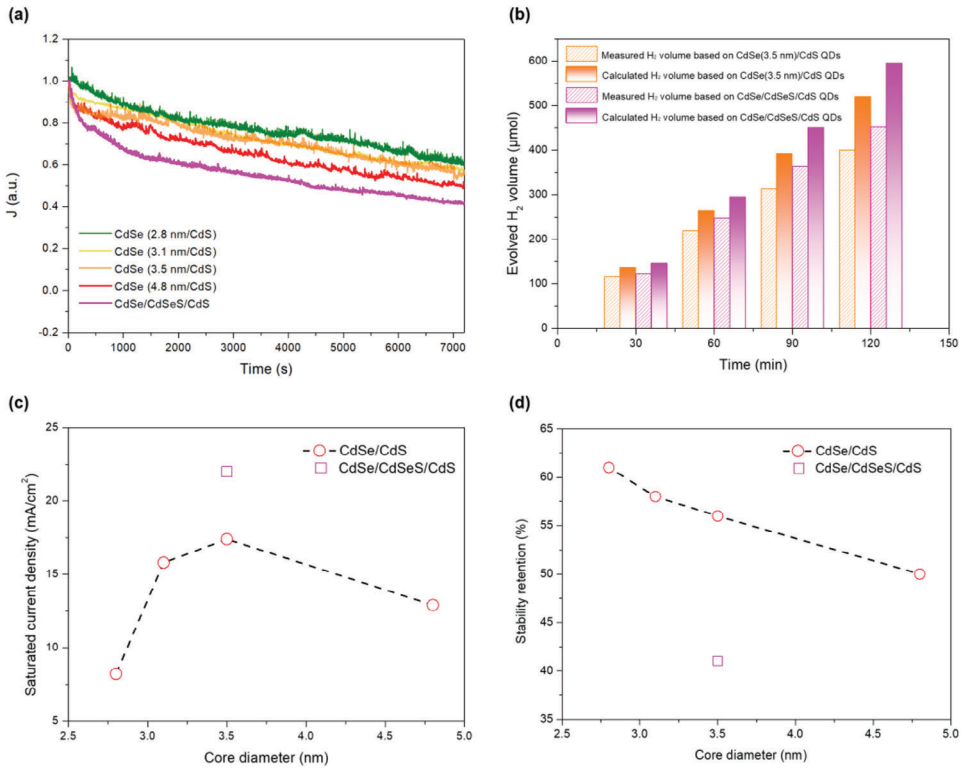

Figure 5. a) Stability measurements (photocurrent density as a function of time) of the four types of CdSe/CdS QDs and alloyed CdSe/CdSeS/CdS QDs-based photoanodes; b) Theoretical and measured H_2 evolution volume as the function of time for CdSe (3.5 nm)/CdS and CdSe/CdSeS/CdS QDs. All of the above measurements were performed at 0.8 V versus RHE with AM 1.5 G illumination (100 mW cm^{-2}). c) Photocurrent density as the function of core diameters; d) Stability retention as the function of core diameters.

on all the QDs samples via SILAR. In Figure 5a, four types of CdSe/CdS and CdSe/$CdSe_xS_{1-x}$/CdS alloyed QDs are measured for 2 h. The stability results indicate that the alloyed QDs have the worst stability performance, as only 41% of the initial photocurrent value is maintained after 2 h. Such lower stability retention value compared to pure-shell QDs is mainly because that favorable gradient band can facilitate a faster carrier transfer rate, but also brings more interfacial traps which causes the charge recombination and photooxidation. For four CdSe/CdS QDs with pure shell, the CdSe (2.8 nm)/CdS QDs-based photoanode has the best stability performance with a retention of 61% of the photocurrent density. The CdSe (3.1 nm)/CdS QDs-based photoanode maintained 58% of the current after 2 h while the CdSe (3.5 nm)/CdS QDs-based photoanode maintained 56% of the initial photocurrent. The CdSe (4.8 nm)/CdS QDs-based photoanode kept only 50% of the initial photocurrent value. Overall, the stability performance decreases with a larger core size (Table 4 and Figure 5d), demonstrating that the carrier transfer efficiency is a critical factor for the stability performance. With lower photocurrent carrier transfer efficiency, there are more recombination events inside the QDs while photo-oxidation will also occur when more holes accumulate on the valence band.[59] Such stability performance results provide useful insights for the design of future core/shell QDs architectures. The most important reasons for the deterioration are photo corrosion and photooxidation from inefficient carrier separation and transfer. Thus, the future direction will focus on the QD-based photoanodes' protection as well as band engineering design in core/shell QDs and QD/MOS.

Finally, gas chromatography (GC) was used to measure the evolved H_2 volume. By comparison, with the theoretical volume (details in the experimental part), the Faradic efficiency can be estimated. As shown in Figure 5b, the measured and theoretical volume of H_2 evolved as a function of time (2 h) under continuous one-sun illumination was collected. By the calculations following the equation in the experimental part, the η_{FE} is ≈83%–84% for CdSe (3.5 nm)/CdS and CdSe/CdSeS/CdS QDs with 1-h measurements, respectively. The side effect is mainly attributed to the reduction reaction between electrons and unstable intermediates from Na_2S/Na_2SO_3 electrolyte and the system leakage.

3. Conclusion

In summary, we designed and fabricated four types of CdSe/CdS core/shell QDs via wet chemical synthesis. By controlling different core sizes while maintaining the same shell thickness, the core/shell band alignment as well as the absorption range can be tuned accordingly. As a result, the carrier dynamic behavior inside the QDs and the PEC performance can be dramatically affected. When the four types of core/shell QDs were applied as sensitizers of TiO_2 photoanodes for solar-driven PEC H_2 generation, we obtained the following values of J_{ph}: 8.2 mA cm^{-2} for CdSe (2.8 nm)/CdS QDs, 15.8 mA cm^{-2} for CdSe (3.1 nm)/CdS QDs, 17.4 mA cm^{-2} for CdSe (3.5 nm)/CdS

QDs, and 12.9 mA cm^{-2} for CdSe (4.8 nm)/CdS QDs, respectively. Thus, the CdSe (3.5 nm)/CdS core/shell QDs-based photoanode shows the optimized PEC performance among four core sizes. This is mainly because the QDs have an enhanced absorption range compared to QDs with smaller cores while maintaining a good charge transfer efficiency when compared with larger cores. Finally, based on the core size of 3.5 nm QD, alloyed CdSe/CdSeS/CdS QDs were designed to further improve the PEC performance by optimizing the shell composition. Thanks to the additional gradient shell, a J_{ph} as high as 22 mA cm^{-2} can be obtained, which is at the top of the list for PEC H_2 generation based on all colloidal QDs-based photoanodes. These results indicate that the CdSe/CdS architecture with proper core size and band alignment can be a promising photoanode for efficient PEC H_2 generation. More importantly, such band engineering approaches based on the core size effect are promising for future high-performance optoelectronic devices.

4. Experimental Section

Materials: Oleic acid (OA, 90%), alpha-terpineol octadecene (ODE, >97%), oleylamine (OLA, 80%–90%), sodium sulfide nonahydrate ($Na_2S{\cdot}9H_2O$), sodium sulfite (Na_2SO_3), zirconium oxide (ZrO_2), Cadmium oxide (CdO) were purchased from Sigma-Aldrich Inc. Trioctyl phosphine (TOP, 90%), cetyltrimethyl ammonium bromide (CTAB), zinc acetate dihydrate [$Zn(CH_3COO)_2{\cdot}2H_2O$], titanium tetrachloride ($TiCl_4$) were obtained from Aladdin Inc. Sulfur powder (S, >99.5%), selenium pellet (Se, >99.999%), trioctylphosphine oxide (TOPO, 90%) were acquired from Macklin Inc. Toluene, methanol, ethanol, and isopropanol (IPA) were bought from Chinasun Specialty Products Co., Ltd. The mesoporous TiO_2 films were prepared by using commercial TiO_2 pastes from Greatcell Solar Materials Pty Ltd, including 18 NR-T paste (≈20 nm in diameter) as a transparent layer and 18 NR-AO paste as a scattering layer (20–450 nm in diameter). No additional purification was done before using the compounds and solvent.

Synthesis of QDs: We used the hot-injection method to synthesize the four types of CdSe core QDs with different sizes. Typically, Se-ODE (0.2 M) was quickly injected into the $Cd(OA)_2$ (0.4 mmol CdO powder with 5 mL oleic acid in 10 mL ODE) at 300 °C. After the injection, the temperature was adjusted to 260 °C for the growth of the nanocrystals. After maintaining different reaction times (1, 2.5, 3.5, and 5 min for four QDs), cold water was used to stop the growth of the CdSe core QDs. Then ≈20 mL ethanol was added into the mixtures of reactants to purify QDs at least four times under centrifugation of 10,000 r.p.m. for 5 min. For each purification cycle, 1:1 (v:v) ethanol/toluene was used and finally, the QDs were dispersed in toluene with a concentration of ≈10 mg mL^{-1} for further usage.

The successive ion layer adsorption and reaction (SILAR) approach was used to grow the CdS shell with a controllable thickness on the CdSe core QDs. Before growing the shell, the diameter and concentration of the core were estimated through the empirical mathematical functions as shown below:

$$D = \left(1.6122 \times 10^{-9}\right)\lambda^4 - \left(2.6575 \times 10^{-6}\right)\lambda^3 + \left(1.6242 \times 10^{-3}\right)\lambda^2 - (0.4277)\,\lambda + (41.57) \quad (3)$$

Generally, the CdS shell was deposited on the CdSe seed by calculating the amount of precursors for each layer. The initial volume of CdSe seed was ≈2×10^{-7} mol with a concentration of 10 mg mL^{-1} while 0.2 M $Cd(OA)_2$ and 0.2 M S-ODE were used as the cation/anion precursors. The injection amount for each SILAR cycle is listed in Table S1 (Supporting Information). For the adsorption time, $Cd(OA)_2$ was kept for 60 min while S-ODE was kept for 10 min for each cycle. The reaction temperature was maintained under 240 °C. After the last cycles of the SILAR process, an extra 10-min annealing was further applied for better crystallization. For the synthesis of alloyed CdSe/CdSeS/CdS QDs, the procedure was similar but using Se/S-ODE (1/1, M/M) as the anion precursor. The purification process of core-shell QDs was applied following the same procedure as core QDs and 10 mg mL^{-1} core-shell QDs were redispersed in toluene for further usage.

Anode Preparation: First, the FTO was carefully cleaned in an ultrasonic machine for 40 min with isopropanol, ethanol, and deionized water, respectively. After the cleaning process, the same solvent was used to rinse the FTO surface to remove the residuals. Finally, N_2 gas was used to dry the FTO. For depositing the TiO_2 blocking layer, $TiCl_4$ aqueous solution (50 mM) was used as a precursor. Generally, clean FTO was immersed into the $TiCl_4$ solution in a glass petri dish. Subsequently, the petri dish was placed in an oven at 70°C for 30 min. The FTO was then rinsed with water and ethanol slowly. Finally, the anodes were dried in N_2 flow and annealed under 500 °C for 30 min with an increase rate of 5 °C min^{-1}. For the deposition of TiO_2 mesoporous films, tape casting was used by applying the TiO_2 paste containing 20 nm particles and mixed particles (20–450 nm) as the transparent layer and scattering layer, respectively. Similarly, the anodes were then annealed at 500 °C for 30 min.

EPD and Passivated ZnS Layer Capping: To deposit the as-prepared QDs into mesoporous TiO_2 films, the EPD approach was employed. Usually, two anodes were positioned vertically inside the QDs solution under a bias of 200 V for 120 min. Then, toluene was used to remove any QDs on the surface, and N_2 flow was used to dry the anodes. The ligand exchange of the ZnS layer was carried out prior to the PEC measurements. Specifically, 0.1 M methanolic CATB solution was used as the precursor in which the photoanodes were placed for 1 min dipping, then rinsed with methanol and toluene, and finally dried under N_2 flow. To complete the ligand exchange process, two cycles are required. Furthermore, the anodes were capped with a ZnS passivation layer according to the following protocol: the above anodes were first immersed into the 0.1 M of Zn^{2+} solution [$Zn(CH_3COO)_2{\cdot}2H_2O$] in methanol for 1 min, then rinsed with methanol and dried with N_2 flow; subsequently, the anodes were further immersed into the 0.1 M S^{2-} solution ($Na_2S{\cdot}9H_2O$) in methanol/water (1/1 v/v) for 1 min, then rinsed with methanol/water and dried with N_2 flow. In this study, the anodes underwent two cycles to grow capping layers.

Characterization: TEM images, high-resolution TEM (HRTEM) images, and SAED patterns were acquired using an FEI Tecnai TF20. Scanning electron microscopy (SEM) images and EDS mapping were acquired using a scanning electron microscope (Supera 55 Zeiss). X-ray diffraction (XRD) patterns were acquired using a powder X-ray diffractometer (Bruker D8) with Ni-filtered Cu K_α radiation. UV–vis spectra of QDs were recorded on a Perkin Elmer model Lambda 750. Photoluminescence (PL) spectra of QDs were recorded on Fluorescence Spectrometer (NIR-VIS, FL3) with excitation at 400 nm. To determine the average lifetime of the QDs in solution and QDs-TiO_2 (or ZrO_2) films, time-correlated single-photon counting (TCSPC) mode was used under the same facility with a 455 nm laser (1 MHz). DAS6 software was used to fit the raw data.

UPS was conducted using an ultra-pure He gas (He Iα, 21.22 eV) discharge lamp with a total instrumental energy resolution of 0.05 eV. A standard Au film with a work function of −5.1 eV was used as the reference to calibrate the Fermi level and a bias voltage of −5 V was applied to samples to assist the electrons in overcoming the work function of the instrument. All the QDs dispersed in toluene were deposited uniformly on the Si substrate using the spin coating method. The prepared samples were first put into a shaded and sealed container filled with nitrogen and then transferred to the load-lock chamber of the UHV system. The sample preparation and transfer process was carried out under the protection of nitrogen gas to avoid the exposure of samples to ambient air and contamination. For the energy levels calculated from UPS measurement, the equations below were applied:

$$E_F = E_h - 21.21\ \text{eV} \quad (4)$$

$$E_{VB} = E_F - E_I \quad (5)$$

$$E_{CB} = E_{VB} + E\ (\text{bandgap}) \quad (6)$$

The PEC performance of QDs-based photoanodes was tested using an electrochemical workstation (CHI 760) in a three-electrode system. All potentials in the measurement were converted to the RHE in accordance with the following equation using a typical Ag/AgCl electrode as a reference electrode:

$$V_{RHE} = V_{Ag/AgCl} + 0.197 + pH \times 0.059 \quad (7)$$

A Xenon High Brightness Cold Light Source (XD300) fitted with an AM 1.5 filter served as the solar simulation power source. Before every measurement, the intensity of the light power is calibrated at one sun illumination (100 mW cm^{-2}). Nonconductive epoxy was used to cover the photoanode's working surface, leaving a ≈0.12 cm^2 active area exposed to the center of the irradiation.

Using nitrogen (N_2) as a carrier gas, Gas chromatography (Techcomp GC-7900) with a thermal conductivity detector (TCD) was employed to analyze the evolution of H_2. At intervals of 30 min, the 0.6 mL of gas sample was extracted from the PEC system's sealed chamber using an airtight syringe and then fed into the GC. The Faradaic efficiency η_{FE} is calculated based on the equation:

$$\text{Faradaic efficiency} \quad (\eta_{FE}) = \frac{V\ measured\ gas}{V\ calculated\ gas} \quad (8)$$

The incident photon-to-photocurrent efficiency (IPCE), which is wavelength-dependent, was determined using the following equation:

$$IPCE\ (\%) = \frac{1240\,J}{\lambda \times I} \times 100\% \quad (9)$$

Where J stands for the photocurrent density (mA cm^{-2}), λ represents the wavelength of incident light (nm), and I denotes the intensity of the incident light (mW cm^{-2}).

Supporting Information

Supporting Information is available from the Wiley Online Library or from the author.

Acknowledgements

This work was supported by the National Nature Science Foundation of China (Grant No. 12275190) and the National Science and Technology Major Project from the Minister of Science and Technology of China (Grant No. 2018AAA0103104). This work was also supported by the Collaborative Innovation Center of Suzhou Nano Science & Technology, the Priority Academic Program Development of Jiangsu Higher Education Institutions (PAPD), the 111 Project, Joint International Research Laboratory of Carbon-Based Functional Materials and Devices. H.Z. acknowledges support from Shandong Natural Science Funds for Distinguished Young Scholar (Grant No. ZR2020JQ20) and the Youth Innovation Team Project of Shandong Provincial Education Department. F.R. is grateful to the Canada Research Chairs program for partial salary support and to NSERC for an individual Discovery Grant.

Conflict of Interest

The authors declare no conflict of interest.

Author Contributions

K. W. and Y. T. contributed equally to this work. K.W. synthesis and characterization of QDs, PEC measurement, data analysis, and manuscript writing. Y.T.: synthesis and characterization of QDs, EDS mapping, UPS measurement, PEC measurement. Z. T. and X. Xu: PEC and stability measurement. F. V.: simulation of the wavefunctions of QDs. D. B., H.Z., X.S., and F. R. supervised the work and edited the manuscript.

Data Availability Statement

The data that support the findings of this study are available from the corresponding author upon reasonable request.

Keywords

absorption range, band alignment, carrier transfer efficiency, core size effect, Photoelectrochemical hydrogen generation

Received: July 29, 2023
Revised: November 12, 2023
Published online: November 30, 2023

[1] M. Grätzel, *Nature* **2001**, *414*, 338.
[2] Y. Tachibana, L. Vayssieres, J. R. Durrant, *Nat. Photon.* **2012**, *6*, 511.
[3] X. Chen, S. Shen, L. Guo, S. S. Mao, *Chem. Rev.* **2010**, *110*, 6503.
[4] L. J. Minggu, W. R. Wan Daud, M. B. Kassim, *Int. J. Hydrogen Energy* **2010**, *35*, 5233.
[5] A. Fujishima, K. Honda, *Nature* **1972**, *238*, 37.
[6] S. C. Warren, K. Voïtchovsky, H. Dotan, C. M. Leroy, M. Cornuz, F. Stellacci, C. Hébert, A. Rothschild, M. Grätzel, *Nat. Mater.* **2013**, *12*, 842.
[7] O. K. Varghese, D. Gong, M. Paulose, K. G. Ong, E. C. Dickey, C. A. Grimes, *Adv. Mater.* **2003**, *15*, 624.
[8] K. Basu, H. Zhang, H. Zhao, S. Bhattacharya, F. Navarro-Pardo, P. K. Datta, L. Jin, S. Sun, F. Vetrone, F. Rosei, *Nanoscale* **2018**, *10*, 15273.
[9] Y. Tao, Z. Tang, Y. Zhong, D. Bao, Z. Gao, W. Zhao, Z. Wen, H. Zhang, K. Wang, X. Sun, *J. Mater. Chem. A* **2023**, *11*, 15833.
[10] J. Deng, X. Lv, J. Gao, A. Pu, M. Li, X. Sun, J. Zhong, *Energy Environ. Sci.* **2013**, *6*, 1965.
[11] A. P. Alivisatos, *Science* **1996**, *271*, 933.
[12] H. Zhao, F. Rosei, *Chem* **2017**, *3*, 229.
[13] H. Zhao, R. Sun, Z. Wang, K. Fu, X. Hu, Y. Zhang, *Adv. Funct. Mater.* **2019**, *29*, 1902262.
[14] F. P. García De Arquer, D. V. Talapin, V. I. Klimov, Y. Arakawa, M. Bayer, E. H. Sargent, *Science* **2021**, *373*, eaaz8541.
[15] L. Jin, H. Zhao, Z. M. Wang, F. Rosei, *Adv. Energy Mater.* **2021**, *11*, 2003233.
[16] M. Zamkov, *Nat. Energy* **2017**, *2*, 17072.
[17] Z. Lin, A. Franceschetti, M. T. Lusk, *ACS Nano* **2011**, *5*, 2503.
[18] F. Navarro-Pardo, H. Zhao, Z. M. Wang, F. Rosei, *Acc. Chem. Res.* **2018**, *51*, 609.
[19] K. Zhao, Z. Pan, X. Zhong, *J. Phys. Chem. Lett.* **2016**, *7*, 406.
[20] S. Kim, B. Fisher, H.-J. Eisler, M. Bawendi, *J. Am. Chem. Soc.* **2003**, *125*, 11466.
[21] Z. Pan, H. Zhang, K. Cheng, Y. Hou, J. Hua, X. Zhong, *ACS Nano* **2012**, *6*, 3982.
[22] R. Xie, X. Zhong, T. Basché, *Adv. Mater.* **2005**, *17*, 2741.
[23] P. Reiss, M. Protière, L. Li, *Small* **2009**, *5*, 154.
[24] D. Benetti, D. Cui, H. Zhao, F. Rosei, A. Vomiero, *Small* **2018**, *14*, 1801668.
[25] L. Jin, B. Alotaibi, D. Benetti, S. Li, H. Zhao, Z. Mi, A. Vomiero, F. Rosei, *Adv. Sci.* **2016**, *3*, 1500345.
[26] L. Jin, G. Sirigu, X. Tong, A. Camellini, A. Parisini, G. Nicotra, C. Spinella, H. Zhao, S. Sun, V. Morandi, M. Zavelani-Rossi, F. Rosei, A. Vomiero, *Nano Energy* **2016**, *30*, 531.
[27] J. Liu, H. Zhang, F. Navarro-Pardo, G. S. Selopal, S. Sun, Z. M. Wang, H. Zhao, F. Rosei, *Appl. Surf. Sci.* **2020**, *530*, 147252.
[28] R. Adhikari, K. Basu, Y. Zhou, F. Vetrone, D. Ma, S. Sun, F. Vidal, H. Zhao, F. Rosei, *J. Mater. Chem. A* **2018**, *6*, 6822.

[29] R. Adhikari, L. Jin, F. Navarro-Pardo, D. Benetti, B. Alotaibi, S. Vanka, H. Zhao, Z. Mi, A. Vomiero, F. Rosei, *Nano Energy* **2016**, *27*, 265.
[30] F. Navarro-Pardo, X. Tong, X. Tong, G. S. Selopal, S. G. Cloutier, S. Sun, A. C. Tavares, H. Zhao, Z. M. Wang, F. Rosei, *Appl. Catal. B* **2019**, *245*, 167.
[31] H. Zhang, L. V. Besteiro, J. Liu, C. Wang, G. S. Selopal, Z. Chen, D. Barba, Z. M. Wang, H. Zhao, G. P. Lopinski, S. Sun, F. Rosei, *Nano Energy* **2021**, *79*, 105416.
[32] K.-H. Lin, C.-Y. Chuang, Y.-Y. Lee, F.-C. Li, Y.-M. Chang, I.-P. Liu, S.-C. Chou, Y.-L. Lee, *J. Phys. Chem. C* **2012**, *116*, 1550.
[33] Y.-L. Lee, Y.-S. Lo, *Adv. Funct. Mater.* **2009**, *19*, 604.
[34] X. Tong, X.-T. Kong, Y. Zhou, F. Navarro-Pardo, G. S. Selopal, S. Sun, A. O. Govorov, H. Zhao, Z. M. Wang, F. Rosei, *Adv. Energy Mater.* **2018**, *8*, 1701432.
[35] X. Tong, Y. Zhou, L. Jin, K. Basu, R. Adhikari, G. S. Selopal, X. Tong, H. Zhao, S. Sun, A. Vomiero, Z. M. Wang, F. Rosei, *Nano Energy* **2017**, *31*, 441.
[36] B. Luo, J. Liu, H. Guo, X. Liu, R. Song, K. Shen, Z. M. Wang, D. Jing, G. S. Selopal, F. Rosei, *Nano Energy* **2021**, *88*, 106220.
[37] F. Li, M. Zhang, D. Benetti, L. Shi, L. V. Besteiro, H. Zhang, J. Liu, G. S. Selopal, S. Sun, Z. Wang, Q. Wei, F. Rosei, *Appl. Catal. B* **2021**, *280*, 119402.
[38] Z. Li, A. I. Channa, Z. M. Wang, X. Tong, *Small* **2023**, 2305146.
[39] N. Zhou, H. Zhao, X. Li, P. Li, Y. You, M. Cai, L. Xia, H. Zhi, A. I. Channa, Z. M. Wang, X. Tong, *ACS Mater. Lett.* **2023**, *5*, 1209.
[40] K. Gong, D. F. Kelley, *J. Chem. Phys.* **2014**, *141*, 194704.
[41] Y. Wang, V. D. Ta, Y. Gao, T. C. He, R. Chen, E. Mutlugun, H. V. Demir, H. D. Sun, *Adv. Mater.* **2014**, *26*, 2954.
[42] G. S. Selopal, H. Zhao, G. Liu, H. Zhang, X. Tong, K. Wang, J. Tang, X. Sun, S. Sun, F. Vidal, Y. Wang, Z. M. Wang, F. Rosei, *Nano Energy* **2019**, *55*, 377.
[43] W. K. Bae, L. A. Padilha, Y.-S. Park, H. Mcdaniel, I. Robel, J. M. Pietryga, V. I. Klimov, *ACS Nano* **2013**, *7*, 3411.
[44] D. J. Norris, A. L. Efros, M. Rosen, M. G. Bawendi, *Phys. Rev. B* **1996**, *53*, 16347.
[45] B. O. Dabbousi, J. Rodriguez-Viejo, F. V. Mikulec, J. R. Heine, H. Mattoussi, R. Ober, K. F. Jensen, M. G. Bawendi, *J. Phys. Chem. B* **1997**, *101*, 9463.
[46] R. Ghosh Chaudhuri, S. Paria, *Chem. Rev.* **2012**, *112*, 2373.
[47] K. Wang, X. Tong, Y. Zhou, H. Zhang, F. Navarro-Pardo, G. S. Selopal, G. Liu, J. Tang, Y. Wang, S. Sun, D. Ma, Z. M. Wang, F. Vidal, H. Zhao, X. Sun, F. Rosei, *J. Mater. Chem. A* **2019**, *7*, 14079.
[48] L. Jin, H. Zhao, D. Ma, A. Vomiero, F. Rosei, *J. Mater. Chem. A* **2015**, *3*, 847.
[49] S. Bisschop, P. Geiregat, T. Aubert, Z. Hens, *ACS Nano* **2018**, *12*, 9011.
[50] H. Zhao, Z. Fan, H. Liang, G. S. Selopal, B. A. Gonfa, L. Jin, A. Soudi, D. Cui, F. Enrichi, M. M. Natile, I. Concina, D. Ma, A. O. Govorov, F. Rosei, A. Vomiero, *Nanoscale* **2014**, *6*, 7004.
[51] P. R. Brown, D. Kim, R. R. Lunt, N. Zhao, M. G. Bawendi, J. C. Grossman, V. Bulovic, *ACS Nano* **2014**, *8*, 5863.
[52] H. Zhao, X. Li, M. Cai, C. Liu, Y. You, R. Wang, A. I. Channa, F. Lin, D. Huo, G. Xu, X. Tong, Z. M. Wang, *Adv. Energy Mater.* **2021**, *11*, 2101230.
[53] J. Zhou, M. Zhu, R. Meng, H. Qin, X. Peng, *J. Am. Chem. Soc.* **2017**, *139*, 16556.
[54] N. S. A. Eom, T.-S. Kim, Y.-H. Choa, W.-B. Kim, B. S. Kim, *Mater. Lett.* **2013**, *99*, 14.
[55] K. Wang, J. Liu, Y. Tao, D. Benetti, F. Rosei, X. Sun, *J. Phys. Chem. C* **2022**, *126*, 174.
[56] K. Wang, Y. Tao, Z. Tang, D. Benetti, F. Vidal, H. Zhao, F. Rosei, X. Sun, *Nano Energy* **2022**, *100*, 107524.
[57] Z. Tang, Y. Tao, K. Wang, D. Bao, Z. Gao, H. Zhao, H. Zhang, Z. Wen, X. Sun, *Nano Energy* **2023**, *113*, 108533.
[58] Y. Tao, Z. Tang, D. Bao, H. Zhao, Z. Gao, M. Peng, H. Zhang, K. Wang, X. Sun, *Small* **2023**, *19*, 2206316.
[59] G. Liu, Z. Ling, Y. Wang, H. Zhao, *Int. J. Hydrog. Energy* **2018**, *43*, 22064.